RESEARCH ARTICLE

NANO · MICRO small
www.small-journal.com

Versatile Patterning of Liquid Metal via Multiphase 3D Printing

*Dhanush Patil, Siying Liu, Dharneedar Ravichandran, Sri Vaishnavi Thummalapalli, Yuxiang Zhu, Tengteng Tang, Yuval Golan, Guillaume Miquelard-Garnier, Amir Asadi, Xiangjia Li, Xiangfan Chen, and Kenan Song**

This paper presents a scalable and straightforward technique for the immediate patterning of liquid metal/polymer composites via multiphase 3D printing. Capitalizing on the polymer's capacity to confine liquid metal (LM) into diverse patterns. The interplay between distinctive fluidic properties of liquid metal and its self-passivating oxide layer within an oxidative environment ensures a resilient interface with the polymer matrix. This study introduces an inventive approach for achieving versatile patterns in eutectic gallium indium (EGaIn), a gallium alloy. The efficacy of pattern formation hinges on nozzle's design and internal geometry, which govern multiphase interaction. The interplay between EGaIn and polymer within the nozzle channels, regulated by variables such as traverse speed and material flow pressure, leads to periodic patterns. These patterns, when encapsulated within a dielectric polymer polyvinyl alcohol (PVA), exhibit an augmented inherent capacitance in capacitor assemblies. This discovery not only unveils the potential for cost-effective and highly sensitive capacitive pressure sensors but also underscores prospective applications of these novel patterns in precise motion detection, including heart rate monitoring, and comprehensive analysis of gait profiles. The amalgamation of advanced materials and intricate patterning techniques presents a transformative prospect in the domains of wearable sensing and comprehensive human motion analysis.

1. Introduction

Traditional electronics and sensors are prone to failure under mechanical stress due to issues such as fatigue, limited range of motion, and lack of stretchability, limiting their potential applications.[1–5] As the interest in the field of stretchable electronics, soft robotics, and human-interface devices peaked, there has been an increased focus on this context.[6–9] Current widely used LM, gallium (Ga) alloys, like EGaIn, (75% Ga, 25% In by weight) and gallium indium tin (GaInSn or Galinstan, 68% Ga, 22% In, 10% Sn by weight), have emerged as significant materials in the realm of stretchable electronics and soft robotics.[1,5–7,9,10] Their inherent fluidic nature at nearly room temperature and exceptional physiological compatibility have enabled the development of highly stretchable electronics that maintain their electrical properties even under substantial mechanical deformations.[11–14]

In the presence of an oxidative environment, these LMs undergo instant

D. Patil, S. Liu, D. Ravichandran, Y. Zhu, X. Chen, K. Song
School of Manufacturing Systems and Networks (MSN)
Ira Fulton Schools of Engineering
Arizona State University
Mesa, AZ 85212, USA
E-mail: kenan.song@uga.edu

S. V. Thummalapalli
College of Engineering
University of Georgia
302 E. Campus Rd, Athens, GA 30602, USA

T. Tang, X. Li
The School for Engineering of Matter
Transport and Energy (SEMTE)
Ira Fulton Schools of Engineering
Arizona State University
Tempe, AZ 85281, USA

Y. Golan
Department of Materials Engineering
Ben-Gurion University of the Negev
Beer-Sheva 8410501, Israel

Y. Golan
Ilse Katz Institute for Nanoscale Science and Technology
Ben-Gurion University of the Negev
Beer-Sheva 8410501, Israel

The ORCID identification number(s) for the author(s) of this article can be found under https://doi.org/10.1002/smll.202402432

DOI: 10.1002/smll.202402432

oxidation, resulting in the formation of a thin yet stable oxide layer that adheres to adjacent surfaces, thereby imparting stability.[11,12,15] Their compliant-to-surface fluidic nature, coupled with their highly oxidative behavior, renders LMs compatible with various materials, including metals, ceramics, and polymers.[16–20] For instance, LMs can be seamlessly integrated into polymeric gel inks or embedded within porous textile fibers.[21–23] Furthermore, the majority of LMs possess notably high surface tension (e.g., Hg: 480, EGaIn: 624, and GaInSn: 718 mN m^{-1}), prompting them to naturally adopt a spherical configuration.[24,25] While the protective oxide skin exhibited by LM enhances their conformity to flat, spherical, or uneven surfaces, the precise positioning and ordered patterning of LMs, particularly within composites or hybrid materials, has proven to be a formidable challenge.

Various techniques, including stamping, imprinting, soft lithography, masking, molding, and additive manufacturing, constitute the mainstream approaches for patterning LMs at the time.[26–32] Among these, additive manufacturing amalgamates multiple methods, opening a path for controlled LM patterning, especially through techniques like electrohydrodynamic jet printing (EHD) and direct ink writing (DIW).[33–36] EHD leverages an electric field to generate jets for meticulous deposition. By applying voltage through a fine nozzle, EHD induces the formation of a stable jet that can be accurately positioned on a substrate. Despite its remarkable sub-micron resolution control, EHD encounters challenges in terms of speed and scalability. In contrast, DIW involves the direct deposition of LM through dispensing systems, facilitating the precise fabrication of intricate shapes and patterns.[35,37] The precision of LM patterning using DIW primarily hinges on factors like nozzle size, injection rates, and LM viscosity. For instance, Ga-based alloys with low viscosity can be extruded through fine nozzles, controlled during dispensing, to generate desired patterns.[38] However, both EHD and DIW often operate with single materials at a time, necessitating recalibration of printing parameters for additive layers, which includes adjusting injection rates, travel speed, and drying kinetics.

While all these techniques demonstrate precision in patterning, our focus centers on the versatility offered by multimaterial, multiphase 3D printing, particularly when combined with customized 3D-printed nozzle attachments. We introduced here an innovative 3D printing methodology to achieve diverse topologies in LM patterning. In contrast to conventional DIW techniques that solely deposit LM, our multiphase 3D printing approach facilitated the simultaneous flow of two distinct feedstocks—EGaIn and PVA—through separate nozzle channels. While the non-merged channels allowed linear EGaIn deposition, the other printhead designs featured merged channels, promoting precise contact and interaction between EGaIn and PVA within a confined region termed the crossflow phenomenon.[39,40] Unlike linear deposits, this distinct printhead design enabled the controlled creation of periodic LM droplets, separated by continuous PVA deposits. We carefully optimized the rheological characteristics of EGaIn for successful 3D printability. Our versatile LM patterning method was programmable by adjusting flow pressure and printing speeds, yielding discrete dots, interconnected dots with varying packing densities, and continuous lines. The resulting patterns exhibited exceptional attributes, including high flexibility, and cyclic capacitive stability, rendering them well-suited for wearable sensing applications. Remarkably, our approach prioritizes autonomy and maintains a compact instrument footprint, highlighting its efficiency.

2. Results and Discussion

2.1. 3D Printing Innovation

To facilitate distinctive surface patterning with EGaIn, we developed and manufactured two types of 3D printing nozzles, illustrated in **Figure 1a**, namely "Merged" (M) and "Non-Merged" (NM) (refer to Figures S1–S3, Supporting Information). These nozzles were produced using our in-house micro-Continuous Liquid Interface Production (μCLIP) 3D printing technology, as depicted in Figure $1a_1$.[41] The μCLIP method, a recently advanced photopolymerization-based 3D printing technique, excels in rapidly creating intricate 3D structures with exceptionally smooth surface textures and consistent mechanical properties.[42] This swift and uninterrupted printing process originates from what is known as the "dead zone", situated at the liquid interface between the oxygen-permeable transparent window and the printing platform (Figure $1a_2$). Oxygen presence in this region inhibits the photopolymerization of photo-curable resins, eliminating the need for repetitive delamination during printing. As a result, it ensures both rapid and detail-rich prints.

Our in-house designed nozzles are visually distinguishable based on the way their two channels intersect, as detailed in the SEM images in Figure S1a (Supporting Information) for the NM nozzle and Figure S1b (Supporting Information) for the M nozzle. In Figure $1a_3$, the M channels exhibit in-channel material interactions, while Figure $1a_4$ displays NM channels with in-channel separations, signifying an absence of direct feedstock interaction. Notably, NM channels feature a channel wall that terminates at the nozzle tip, as shown in Figure S2 (Supporting Information), while M's wall concludes 0.5 mm before the nozzle tip, as shown in Figure S3 (Supporting Information). This difference in wall termination creates a junction in M where the two feedstocks interact, establishing a distinct hydrodynamic flow regime. The nozzles efficiently delivered dual feedstocks, denoted as A-PVA and B-EGaIn, via independently regulated pressure flow systems for each feedstock, as illustrated in Figure $1b_1$. Hence the two inlets for each feedstock were consistent in the

G. Miquelard-Garnier
Laboratoire PIMM
CNRS
Arts at Métiers Institute of Technology
Cnam
HESAM Universite
151 Boulevard de l'Hopital, Paris 75013, France
A. Asadi
Department of Engineering Technology and Industrial Distribution
Texas A&M University
College Station, TX 77843-3367, USA
K. Song
School of Environmental
Civil
Agricultural and Mechanical (ECAM)
University of Georgia
Athens, GA 30602, USA

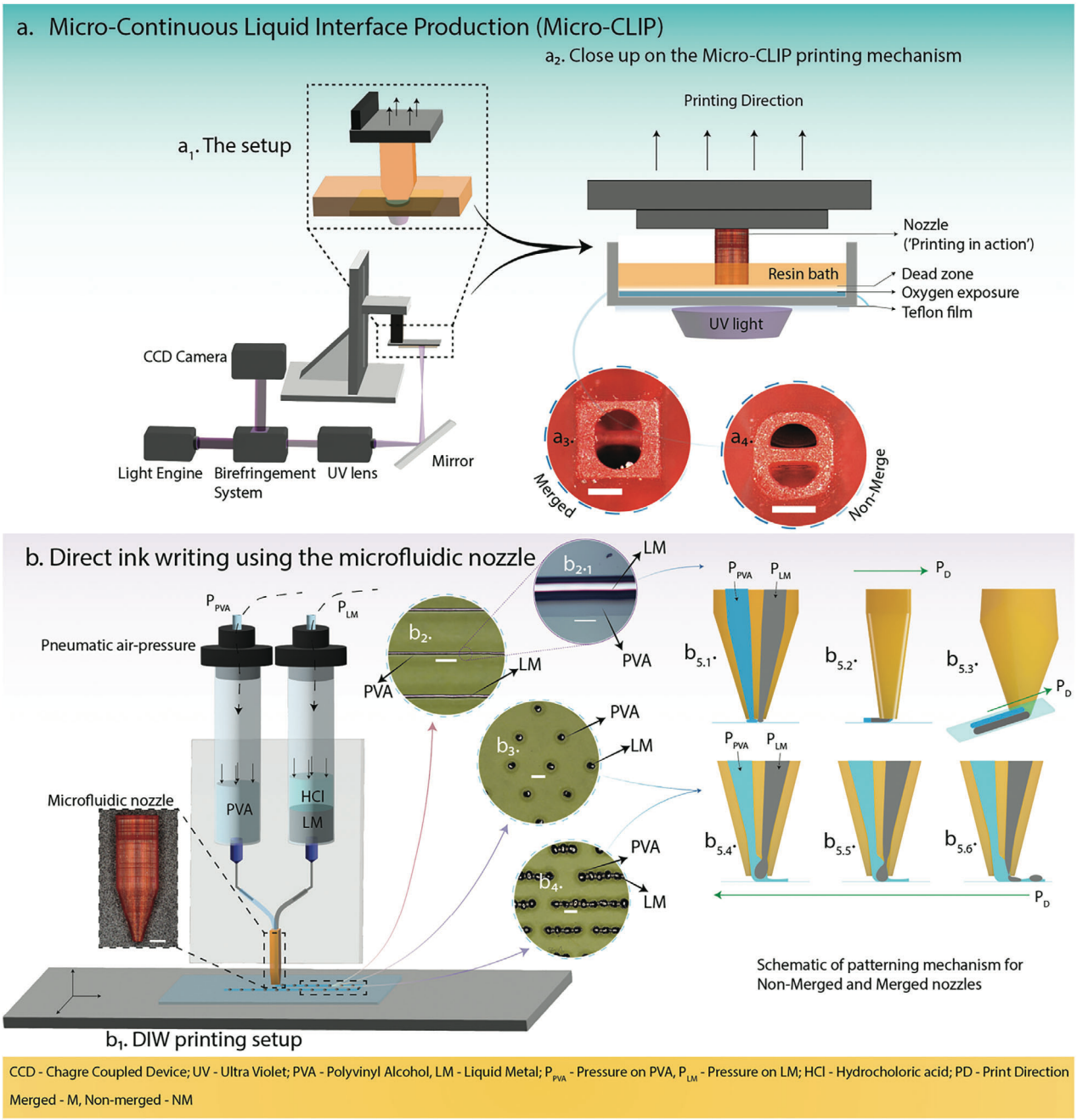

Figure 1. Schematic of the printing platform setup and in-house designed printing nozzle for LM patterning. a_1) The μCLIP printing platform and a_2) the close-up on the μCLIP printing mechanism for a_3) the merged nozzle tip (scale bar – 250 μm) with droplet patterning capabilities and a_4) non-merged nozzle tip (scale bar – 250 μm) for continuous material deposition features. b_1) Schematic showing our multimaterial 3D printing with the μCLIP-processed microfluidic nozzle as a creative printhead (scale bar – 500 μm), capable of, b_2) line arrays patterned using a non-merged nozzle (as shown in a_4) (scale bar – 500 μm), with $b_{2.1}$) a zoomed-in view at the interface between the LM and the PVA in the line arrays (scale bar – 1000 μm) and, b_3,b_4) dotted patterning of different assembly sizes and periodicities (scale bar – 1000 μm) via a merged nozzle (as shown in a_3). $b_{5.1}$–$b_{5.3}$) Schematic cross section of the non-merged nozzle tip to illustrate the printing of line arrays, and $b_{5.4}$–$b_{5.6}$) schematic cross section of the merged nozzle tip showing the formation of droplet deposition of LM for patterning purposes during 3D printing.

designs for the both the nozzles (Figure S4, Supporting Information). In the case of NM, separate channels for each feedstock ran in parallel, resulting in line arrays without intersections, as depicted in Figure 1b_2,$b_{2.1}$. In contrast, the M nozzle featured a crossflow design where the channels intersected, creating droplet patterns that combined PVA with LM, as shown in Figure 1b_3,b_4 (Figure S3, Supporting Information).[40,43] These droplets of EGaIn along with the PVA were deposited onto the glass substrates. Due to the poor wetting behavior of PVA on polyethylene terephthalate (PET) sheets (Figure S5, Supporting

Information), and EGaIn's corrosive response to metallic substrates, glass substrate was used as the suitable substrate for the patterning.[44,45]

In this investigation, EGaIn and PVA illustrate their diverse surface patterning capabilities when dispensed through NM using distinct pneumatic pressures (P_{LM} and P_{PVA}), as detailed in Figure $1b_{5.1–5.3}$. The channel alignment for NM nozzles with respect to the printing direction was set perpendicular to the printing direction. This decision was informed by the evidence from Figure S7 (Supporting Information), where aligning the channels in-line with the printing direction leads to chaotic periodicity. Hence the channel orientation and NM's configuration with non-intersecting channels, EGaIn and PVA remained segregated until their deposition on the substrate. Upon deposition, PVA underwent relaxation, establishing a well-defined interface with the LM, devoid of interfacial diffusion (Figure S8, Supporting Information). EGaIn was deposited as elongated lines alongside PVA on the glass substrate, representing an initial outcome aimed at exploring the patterning potential of the two nozzles, as depicted in Figure $1b_2$. In Figure $1b_{2.1}$, the immiscibility of EGaIn and PVA resulted in distinct phases, consistent with previous reports on microfluidic channels created using EGaIn-DIW, often encapsulated within polymers.[46,47]

The formation of LM lines via DIW is a well explored process attributed to the oxidation phenomenon.[12,38,48] Despite its high surface tension, LM rapidly develops an oxide layer in an oxidative environment, thereby stabilizing its contact with the glass substrate. The wrinkled morphology observed serves as validation of instantaneous oxidation, enhancing the mechanical adhesion at the glass substrate/EGaIn interface and further immobilizing the printed line.[49,50] Simultaneously, the continuous shear of LM allows for extrusion while maintaining contact with the substrate material at the nozzle tip. This phenomenon has enabled researchers to create print-on-demand patterns, such as circuits and antennas.[48,51,52] However, these methods have been confined to DIW, compatible with only one material at a time.

As established, the crossflow design promoted the interaction of the two different liquid phases with varying interfacial energies (EGaIn: 624, and PVA: 36.5–43.3 mN m^{-1}).[40,43] This interaction created an interfacial instability leading to a deformed interface. EGaIn, characterized by its properties, gathered into a pool or an early-stage droplet, acting as the discontinuous phase. Meanwhile, PVA served as the continuous medium, enveloping the aggregated EGaIn, while its flow pressure facilitated EGaIn bulking (Figure $1b_{5.4}$). During the printing process, PVA continued to deposit onto the glass substrate. Over time, the aggregate consumed sufficient EGaIn to start stretching due to the influence of gravity and the flowing PVA, forming a necking region induced by high surface tension and continuous surface oxidation (Figure $1b_{5.5}$). The pinching off of the neck resulted from interfacial instability, the flow of PVA, and the shearing between the flow and the nozzle tip's edge (see Figure $1b_{5.6}$), also documented in Video S1 (Supporting Information). In Figure S8 (Supporting Information), the EGaIn droplet can be seen to be surrounded by PVA. The droplet generation can be termed passive, as the process didn't involve external force fields.[43] Instead, the deformation of the interface was dictated by geometric design, pressure-driven flow, and the immiscibility of the fluids involved.

Building upon the foundational work in DIW and microfluidics for liquid metal printing, our research introduces an innovative approach to EGaIn patterning by combining these technologies with cross-flow droplet generation. Unlike the primarily structural or material assembly focus in previous literature[53,54] our work leverages the unique rheological and surface properties of EGaIn, integrated within a PVA matrix, to create flexible sensors with enhanced functionality. This method, distinct from the conventional deposition in most DIW methods, allows for precise control over pattern formation, addressing the gaps identified in previous studies. By exploring the specific intricacies of liquid metals, particularly their rapid oxidation and distinctive rheological behavior, our work presents a novel perspective in the realm of multiphase 3D printing, significantly advancing the application of liquid metal-polymer composites in the development of flexible sensing technologies.

Existing literature has showcased the production of LM droplets, particularly using EGaIn, with techniques primarily revolving around "hydrodynamic flow focusing" and "ultrasonication".[39,55,56] In the case of flow focusing, emulsion feedstocks were propelled through capillary tubes or microfluidic devices, inducing the shearing of LM droplets (the discontinuous phase) within a continuous phase. In contrast, ultrasonication harnessed sonic waves to disrupt emulsions, fragmenting bulk LM into micro/nano-droplets. However, it's important to note that these prior efforts were not focused on the intentional patterning of LM, and the act of patterning LM onto substrates has received limited attention. This study addresses this specific gap by introducing a novel method that leverages crossflow geometric design within the printhead to generate patterned droplets with versatile topologies. Our 3D printing approach reported in this study distinguishes itself from conventional DIW methods in a fundamental way. Unlike DIW, it doesn't rely on motion breaks to deposit LM droplets; instead, it facilitates continuous writing, resulting in discrete LM droplets carried by continuous PVA on to the glass substrate. Besides providing flexibility and packaging functionality, PVA also plays a crucial role in preventing LM spreading or coalescence, thereby ensuring higher precision in patterning.

2.2. Rheology and 3D Printing Capability

The rheological behavior of feedstocks played a crucial role in ensuring the feasibility and consistency of 3D printing. In the case of EGaIn, significant attention has been devoted to its surface tension and the oxidation characteristics of gallium within the alloy, as illustrated in **Figure 2**a–e and Figure S9 (Supporting Information).[12,57,58] Various studies have examined the impact of surface oxidation on both the surface tension and the autonomous agglomeration of EGaIn, which is consistent with our observation (see reduced agglomeration in Figure S9a,b, Supporting Information).[12,59,60] In an oxidative environment, the formation of a protective gallium oxide (Ga_2O_3) skin (Figure 2a; Figure S9a,b, Supporting Information) occurred nearly instantaneously, with this oxide layer measuring ≈1 nanometer in thickness.[61,62] This skin acted as a barrier, preventing further agglomeration of the EGaIn material. The presence of this oxide layer also becomes visibly apparent through observable

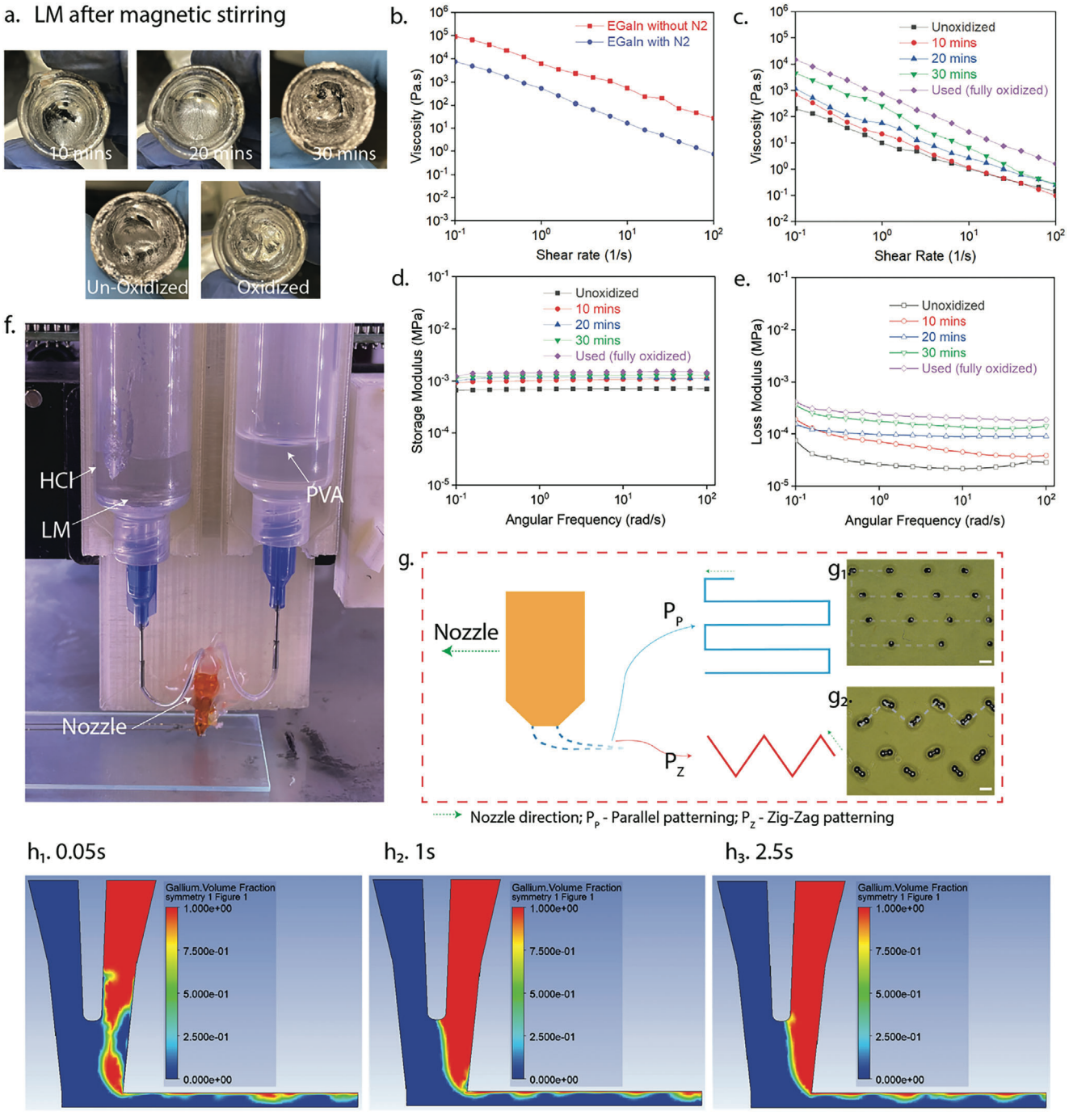

Figure 2. a) Top photos show changes in appearance as a function of stirring durations of 10, 20, and 30 min, and bottom photos compare the unoxidized versus oxidized variants of EGaIn. b) Viscosity versus shear rates of used (oxidized) EGaIn with and without the N_2 atmosphere shows the oxidation effects. c) Viscosity versus shear rates, d) Storage modulus versus angular frequency, and e) loss modulus versus angular frequency of 10 min stirred, 20 min stirred, 30 min stirred, unoxidized, and oxidized variants of EGaIn. f) A close-up photo of the nozzle setup connecting to the material delivery systems (e.g., LM and PVA). g) An illustration to show the different kinds of patterns based on the motion of the nozzle, showing (g_1) regularly spaced droplet patterning – parallel dot arrays because of a straight-line printing path, and g_2) assembled bi-droplet patterning – highly flexible dot assembly with changing zig-zag printing paths (e.g., bi-dot patterning with varying directions of ≈45°/135° for the top and bottom patterning) (scale bar – 1000 µm). h_1 – h_3) ANSYS Fluent simulations optimizing the printing parameters and mimicking the LM-PVA droplet deposition for dotted patterning, see the simulation details in supporting information (Section S1, Supporting Information). Image courtesy of ANSYS, Inc.

wrinkles (Figure 2a), particularly during the shearing of EGaIn.[58] Given that oxidation is an exceedingly rapid process, occurring within mere seconds of exposure to air, we posited that longer stirring durations ranging from 10 to 30 min would induce further oxidation (Figure 2a). Samples subjected to stirring for 10 and 20 min exhibited progressively larger wrinkled areas, while the sample stirred for 30 min achieved a degree of structural stability (Figure S9c vs S9d, Supporting Information), evidenced by smoother wrinkles. Previous researchers have also advocated the oxidation of LM for increased structural stability due to its paste-like nature.[12,50,57,58] Essentially, this process entailed the reaction between O_2 and Ga, leading to the formation of Ga_2O_3 and an increase in its concentration throughout the bulk material. This intriguing phenomenon underpinned the stable formation of upright structures using EGaIn and other gallium-based alloys.[11,61]

However, the introduction of a non-oxidative environment, such as an inert gaseous atmosphere or specific acid or base solutions, had the opposite effect by causing the collapse of the oxide skin, thereby impeding further growth.[60,63] This collapse of the oxide skin led to an increase in the effective interfacial tension, subsequently promoting the agglomeration of LM leading to patterning failure. Consequently, maintaining oxidative conditions within the bulk phase remains critical for establishing stable droplet formation and ensuring consistent patterning. In our particular case, the continuous shearing of the sample through stirring induced the expansion and contraction of EGaIn, resulting in the characteristic appearance of wrinkles.[58] To facilitate this process, we employed the stirring preparation method that continuously disrupted the oxide skin barrier, facilitating ongoing bulk material oxidation. Previous studies have shown that the continuous disruption and reformation of the oxide skin led to increased levels of Ga_2O_3 and a subsequent reduction in effective surface tension, rendering the material printable.[64,65]

EGaIn's non-Newtonian behavior can be attributed to its unique properties.[64,66] Figure 2b,c presents the results of rheological studies, illustrating this non-Newtonian behavior, characterized by a decrease in ink viscosity with increasing shear rate, which corresponds to the shear-thinning phenomenon.[57] The presence of an inert atmosphere (N_2) has been studied to reduce the thickness of the oxide layer, which has an effect on the viscosity of the oxidized sample.[67] As highlighted in Figure 2b, the non-oxidative environment promotes the low viscosity by limiting the oxidation exposure. Figure 2c demonstrates the effect of stirring on viscosity, emphasizing the time-dependent increase in viscosity due to the formation of the shear-induced oxide layer. Reused LMs exhibited the highest viscosity, primarily because of the continuous formation and reformation of the thin oxide layer on the LM's surface during the printing and recycling processes.[68]

Moreover, after oxidation, EGaIn exhibited viscoelastic properties. The oxide film induced elastic behavior until the yield point, beyond which the barrier broke, revealing EGaIn's viscous fluidic behavior.[69] These viscoelastic properties were influenced by the degree of oxidation; more oxidized samples displayed higher storage and loss moduli, as well as yielding stresses (Figure 2d,e). The material storage modulus (E') showed plateaus with increasing frequency (Figure 2d), indicating the material's consistent elastic properties over a range of deformation rates. This suggested that EGaIn's oxide barrier had a stable, frequency-independent yield point, which plastic deformation ensued. The barrier likely engendered elastic behavior until the yield point was reached, benefiting printing consistency. The material loss modulus (E'') also displayed quasi-plateaus as the frequency increased (Figure 2e), indicating consistent viscous properties across various deformation rates, benefiting the flow continuity during printing. More importantly, the more significantly increased loss moduli than the storage moduli as a function of shear frequency suggested that EGaIn's oxide barrier had an improved yield point that was more difficult to have triggered deformation (Figure S9d as compared to S9c, Supporting Information). The barrier likely maintained elastic behavior until reaching this yield point. These rheological characteristics of EGaIn held significant implications for its applications in soft, stretchable electronics and as conductive ink for printing. A comprehensive understanding of EGaIn's multifaceted rheological behavior remains essential for optimizing its performance in these applications.[66]

As mentioned, in an attempt to increase the affinity of the LM to the substrate and printing consistency (Figure S9d, Supporting Information), the prolonged stirring corresponds to increased levels of oxidation facilitating uniform bulk oxidation. However, unlike unoxidized LM, oxidized LM resists the accumulation of liquid to high levels, which can lead to abrupt LM deposition (Figure S9a,b, Supporting Information). Thus, a precisely controlled oxidation would help mitigate this issue, enabling the printing of mechanically durable structures (Figure S9c,d, Supporting Information). For example, following the adjustment of ink rheology for direct ink writing, we set up the feedstocks and the printing apparatus to process premixed LM, as illustrated in Figure 2f. However, we encountered a significant issue: the air stream from the pneumatic dispenser had the potential to create a hole in the LM, leading to a depletion of EGaIn at the nozzle (Figure S10, Supporting Information). To address this problem, it became crucial to fill the syringe with 1–2 mL of hydrochloric acid (HCl) with a pH of 4–5, which not only inhibited further oxidation but also facilitated even distribution of pneumatic air pressure across the exposed surface of the LM.[70,71] Notably, the controlled deposition path in DIW could be programmed to follow the predefined print path. We explored two primary printing paths: parallel and zig-zag patterns, each resulting in distinct patterns (Figure $2g_{1,2}$).

The mechanistic understanding derived from the observed droplet formation mechanism in Figure $1b_{5.4–5.6}$, facilitated by the cross-flow geometry and resulting interfacial instability, was further clarified using fluid dynamics simulation to model fluid behavior and elucidate the underlying patterning mechanism (Figure $2h_{1–3}$). A 2D model representation (Section S1 and Figure S14, Supporting Information) for the simulation effectively validated the experimental observations, enhancing our understanding of the droplet formation process. The color bar from red to blue in Figure $2h_{1–3}$ indicates the gradient intensity of volume fraction of gallium (VF_G) from 1 to 0 in the nozzle during the extrusion. The blue color (representing the PVA volume fraction) appears to have an undisrupted flow (continuous phase). Noticeably, the VF_G in the other channel begins to slump as it interacts with PVA creating a region of interfacial instability. With time the solver reveals the necking region as observed in Figure $1b_{5.4–5.6}$. While droplet formation and deposition occurred

instantaneously, the initial formation required some time. This observation was consistent with the simulation, which indicated periodic droplet deposition occurring ≈2.5 s after initiation.

2.3. Patterning Versatility and Mechanisms

The droplet formation technique introduced in this study presents promising applications in the realm of microelectronics industry or microfluidic devices. It extends its utility beyond mere droplet generation, ushering in new opportunities for spontaneous deposition and the creation of versatile patterns. The explored versatility in this study encompasses the control of droplet spacing through variations in periodicity and the generation of distinctive patterns via alterations in packing density, facilitated by droplet migration seen in **Figures 3** and 4. Achieving this diverse array of patterns through multi-material printing required a profound understanding of rheology and printability. In particular, the investigation delved into the intricate interplay between traverse speed and the influence of flow pressure. Notably, both of these parameters demonstrated significant impacts on droplet spacing, migration, size, and, ultimately, surface pattern diversity (Figure 3a–c).

We first investigated the impact of traverse speed on droplet spacing by varying the speed across a range of 150 to 350 mm min^{-1}. At lower speeds, droplets were deposited closely together, resulting in their migration and accumulation within the PVA domain. As we progressively increased the traverse speed, the migration effects became less pronounced. We established a standardized traverse speed of 250 mm min^{-1} for subsequent printing, primarily because it minimized migration. Further increases in traverse speed resulted in greater droplet spacing (Figure 3d).

Our comprehensive investigation into the impact of flow pressure (P) on droplet spacing revealed that it had a significant influence. Increasing the flow pressure led to a reduction in droplet spacing in both scenarios (Figure 3e,f). For constant P_{PVA} (0.35 bar) and increased P_{LM}, droplet spacing ranged between ≈2 and 8 mm (Figure 3e). Meanwhile, by varying P_{PVA} while keeping P_{LM} constant (0.35 bar), the range expanded to ≈2 and 12 mm (Figure 3f). A closer examination revealed that patterns printed with constant P_{PVA} under increasing P_{LM} exhibited more uniform deposition compared to those produced by varying P_{PVA} at constant P_{LM} (overall smaller deviation in Figure 3e than Figure 3f). Within the specified P_{LM} range of 0.35 to 0.65 bar, while maintaining a constant P_{PVA} of 0.35 bar, analysis revealed the droplet size's interquartile range (IQR) with a variance of 25% to 75% (Figure S11, Supporting Information). As the EGaIn flow pressure increased, we noted a proportional increase in droplet size. The smallest droplet, with an average diameter of 622.05 µm and a variance of 13.01 µm, contrasted with the largest droplet, exhibiting an average diameter of 717.65 µm with a variance of 18.61 µm. This observation is based on meticulous measurements of four distinct droplets within each sample. These findings not only elucidate the direct impact of EGaIn flow pressure on droplet size but also underscore the potential for precise control and optimization of droplet characteristics within the proposed printing framework. Additionally, similar trends wrt. droplet spacing were observed with polydimethyl siloxane (PDMS), which allowed good control over droplet spacing but had limitations in maintaining droplet shape fidelity and deposit extraction (Figure S12, Supporting Information). Due to its lower storage modulus, PDMS caused droplets to settle and adhere to the glass substrate. However, it's worth noting that this method can be adapted to other materials with appropriate modifications. Additionally, the 3D profile of the LM droplet pattern demonstrated the viscoelastic properties of the LM, enabling the retention of its post-deposition shape and structure (Figure 3g_1,g_2). The oxide layer on the surface acted as a barrier that resisted further deformation. This phenomenon contributed to maintaining droplet integrity, facilitating coherent pattern formation.

The versatility of our patterning method was significantly influenced by the interactions among individual LM droplets. For example, a phenomenon termed "droplet migration" was observed (Figure 3a). When the droplets were closely spaced, they exhibited a tendency to migrate, and this migration decreased as the spacing between droplets increased. This phenomenon is similar to the well-known "Cheerios effect", where like objects are attracted to each other on the liquid surface, much like Cheerios cereal pieces gathering at the center of milk in a bowl.[72,73] The Cheerios effect is a surface phenomenon commonly encountered in daily experiences, such as the way air bubbles or tea leaves come together at the liquid's surface.[74] As we delved into our exploration of droplet spacing and printing paths, we uncovered a parallel phenomenon, shedding light on the intricate dynamics and interactions that govern LM droplets.

In our quest to understand this phenomenon and provide a more vivid illustration of droplet migration, we conducted experiments while printing in a zig-zag pattern, as depicted in Figure 4. As observed earlier in Figure 3a, the parallel printing path provided the droplets with unhindered PVA domains that allowed the droplets to migrate. Since, the printing speeds were low, multiple droplets were able to migrate in line within PVA to come in contact with other droplets. In Figure 4a, we offer a detailed breakdown of the mechanism behind the LM droplets moving toward each other. Interestingly, droplet migration commenced just seconds after deposition and continued until the droplets met, completing the migration process. It's worth noting that, although the pool of PVA didn't resemble a typical bowl of milk, it vividly demonstrated the migration phenomenon. Here, when we refer to the "pool of PVA", we are describing the region in which multiple droplets exhibited this migration behavior (Figure 4a1). As we had observed previously, the primary interaction took place at the air-liquid interface when the droplets were partially submerged in the PVA. As the droplets moved without trace marks on the substrate surface, it was an evidence of PVA preventing their contact with the substrate surface.

Furthermore, the migration of EGaIn droplets can be attributted to the density difference between the droplets and the surrounding PVA, with EGaIn being six times denser. This density contrast induces a deformation in the meniscus. The migration process is driven by a delicate balance of horizontal and vertical forces aimed at minimizing this deformation.

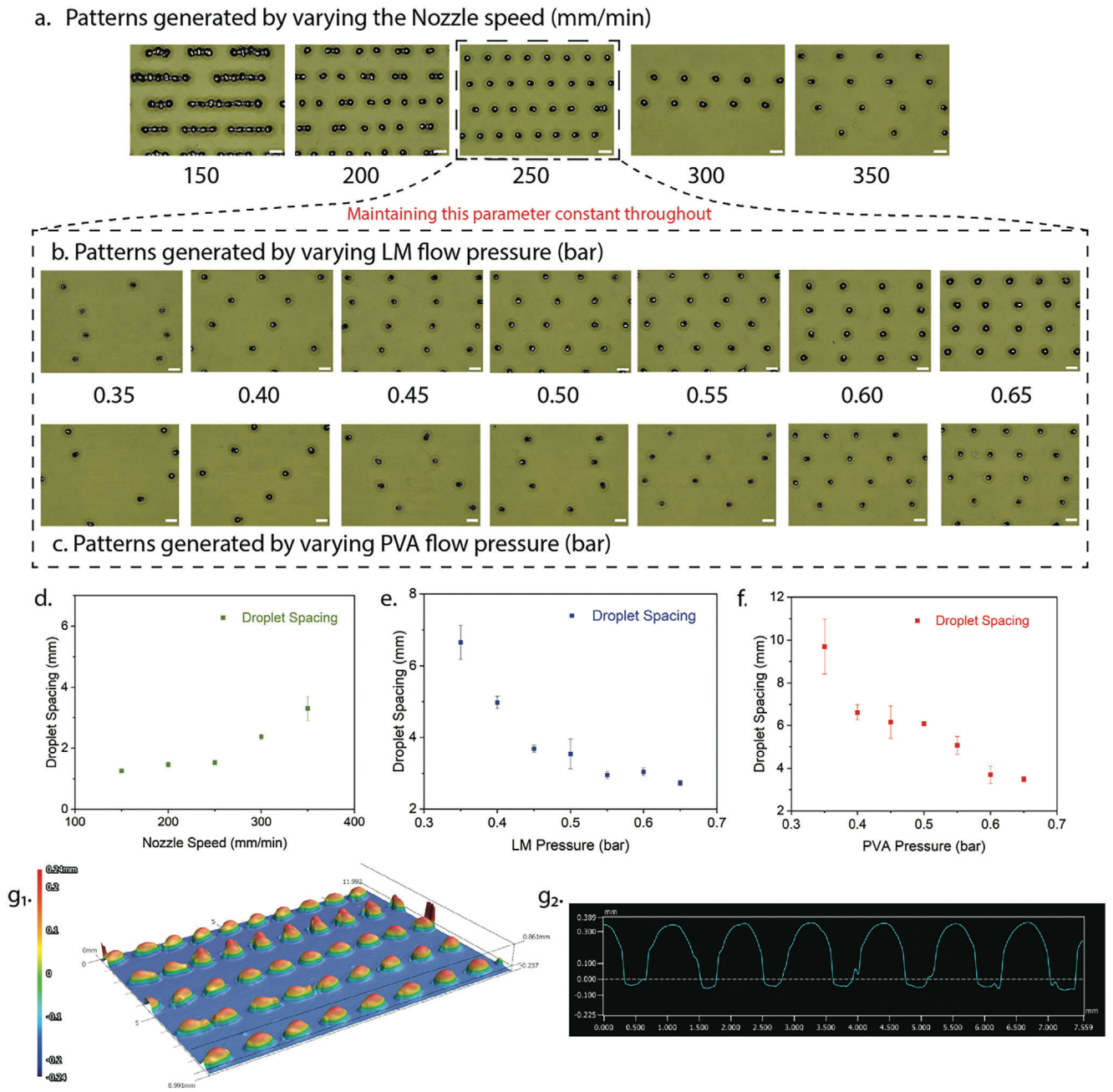

Figure 3. Optical images show LM patterns obtained by a) programming traverse speeds between 150– 350 mm min^{-1} at EGaIn and PVA pressure of 0.5 bar, and at a rate of 250 mm min^{-1} with b) varying EGaIn flow pressure (P_{LM}), and c) changing PVA flow pressure (P_{PVA}), generating highly uniform surface patterns. Quantitative plots of patterning features, namely, the droplet spacing as a function of d) traverse speed, e) P_{LM}, and f) P_{PVA}., show higher patterning resolutions with lower traverse speed, higher EGaIn pressure, and higher PVA pressure. g_1) 3D profile mapping of one EGaIn pattern as an example (i.e., traverse speed of 250 mm min^{-1}, EGaIn pressure of 0.65 bar, and PVA pressure of 0.5 bar). g_2) The height profile along one row of droplets shows the patterning consistency during 3D printing. (Scale bars for a–c – 1000 µm).

The gravitational force (illustrated by the purple arrow), buoyancy (represented by the green arrow), and the vertical component from the surface tension (red arrow) work together to maintain the droplets suspended, as depicted in (Figure 4a2). The restoring forces, stemming from surface tension (depicted by the red arrow & Figure S8, Supporting Information), then push the droplets along the meniscus, gradually bringing them closer. It's worth noting that the extent of droplet migration is contingent on the initial distance between the droplets, with a limitation of 1.5 mm within the same PVA domain, as shown Figure $4b_{1,2}$. The prevalence of this migration within the defined range can be established. Previous literature has highlighted the attractive force between two spheres, which is proportionate to the quantity Σ^2 (Section S3, Supporting Information).[73]

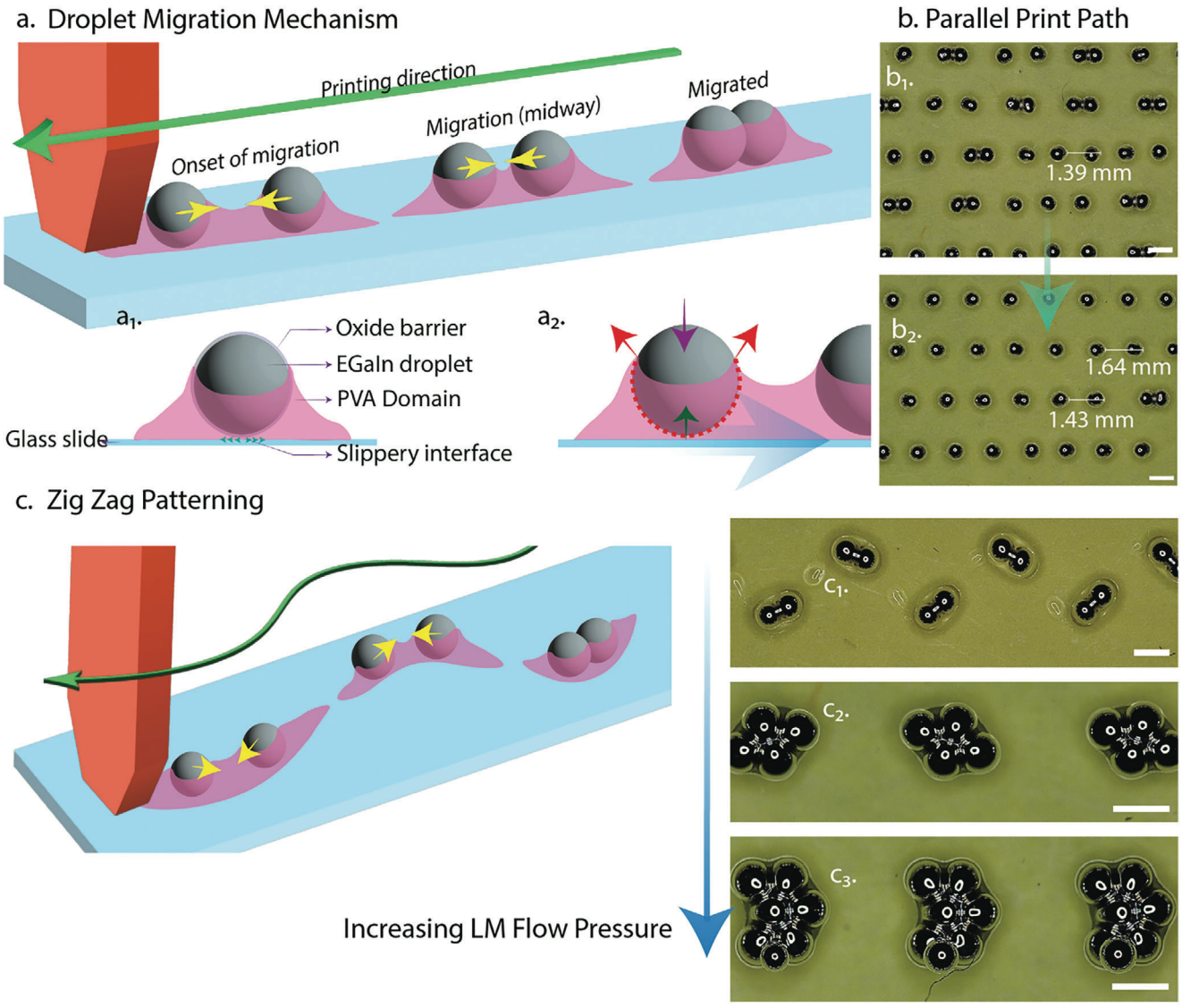

Figure 4. The migration of droplets for versatile LM patterning. a) The mechanism of droplet migration along parallel printing path with a_1) schematic showing a detailed depiction of LM droplet within the surrounding PVA domain and a_2) forces acting on the droplet, including surface tension (red arrow 45°/135° directions), phase interfacial interactions (dashed red curve), gravity (purple arrow downward), and buoyancy (green arrow upward), resulting in the net force that drives the droplet's motion (free body diagram). b_1,b_2) Parallel patterning and fading migration observation by increasing printing speeds from (b_1) 200 mm min^{-1} (i.e., some droplet migrations and coalescences) to (b_2) 250 mm min^{-1} (i.e., no droplet migrations and consistent patterning) at 0.5 bar of P_{LM} and P_{PVA}. c) The mechanism of droplet migration along zig-zag printing paths with c_1) bi-dot patterning, c_2) quad-dot patterning, and c_3) hexa-dot patterning facilitated by migrating multiple droplets for patterning diversity. 3D printing parameter for c_1–c_3: printing speed of 200 mm min^{-1}, with gradual increase of P_{LM} from 0.5 to 0.65 bar, and P_{PVA} of 0.5 bar (scale bar – 1000 µm for c_1–c_3).

A larger Σ^2 corresponds to a stronger attractive force between droplets. This equation underscores the significance of droplet density relative to the surrounding liquid; a higher droplet density implies a stronger attraction. There exists, however, a limit beyond which a droplet cannot remain afloat over PVA. While a droplet can stay buoyant by displacing an amount of PVA to counterbalance its weight, this is constrained by a maximum density ratio, denoted as D_{max}. This ratio defines the highest possible droplet density, under the assumption that a droplet, considered as a sphere of radius r, remains buoyant, as expressed in Equation (1).[72] Here, ρ_{PVA} and ρ_{Air} are the densities of PVA and air, and $\gamma_{Air/PVA}$ is the surface tension at Air/PVA interface.

$$D_{max} = \frac{3}{4}\left(\frac{\gamma_{\frac{Air}{PVA}}}{\left(\rho_{PVA} - \rho_{Air}\right) g}\right)\frac{1}{r^2}\left(1 - cos\theta\right) \quad (1)$$

$$D = \frac{\rho_{LM}}{\rho_{PVA}} \quad (2)$$

Notably, EGaIn droplets, despite their relatively high density of 6.25 g cm^{-3}, display buoyant behavior. When we calculate

the density ratio (D) using Equation (2), we find that D equals 5.25 (Equation (2)), which is still within the permissible limit, considering the maximum density ratio (D_{max}) approaches 6.19. This means that the surrounding PVA can indeed provide sufficient buoyant support to keep the droplets afloat.[74] The attractive forces responsible for this buoyancy originate from the induced deformation of the meniscus, a phenomenon that extends beyond interactions between just two droplets.

The zig-zag patterning (Figure 4c) observed in our study emerged as a result of intricate control over key parameters, specifically the flow pressure of EGaIn, the printing speed, and the printing path. The observed curvature in the zig-zag pattern not only accentuated the Cheerios effect but also introduced a unique geometry that influenced the migration and distribution of droplets. Through deliberate manipulation of P_{LM} within the range of 0.5 to 0.65 bar, while maintaining a constant P_{PVA} of 0.5 bar and a print speed of 200 mm min^{-1}, we achieved systematic variations in droplet population within the PVA pool. This dynamic relationship between P_{LM}, print speed, and droplet distribution played a pivotal role in shaping the intricate zig-zag patterns observed in Figure 4c_{1-3}. The Cheerios effect, driven by the interplay of surface tension and droplet interactions, was harnessed to facilitate the aggregation of droplets, particularly within the curved structure introduced by the zig-zag patterning. The interplay of these parameters showcases the versatility of our approach in achieving controlled and intricate patterns, providing a valuable foundation for further exploration and applications in advanced printing technologies.

2.4. LM Patterning for Capacitive Sensors

In the landscape for stretchable electronics and flexible sensors, capacitive sensors stand out for their simple yet effective design that typically consisted of two conductive plates separated by a dielectric material. These devices excel in their energy efficiency, low detection limit, and wide range applications. But, due to the poor sensitivity in the low pressure ranges, several studies have shown two methods for enhanced performance.[75–77] These methods are categorized as i) elastomeric microstructures and ii) conductive fillers in dielectric polymers. In our case these sensors employ LM droplet patterns, which as conductive elements (EGaIn conductivity of $3.4 \times 10^6 Sm^{-1}$), enhance the dielectric permittivity and, by extension, the capacitance of the composite in which they are embedded.[78,79] Confinement in a polymer matrix, like PVA, and a subsequent PDMS overlay, not only secures the LM in place but also fortifies the sensor's structural integrity (illustrated in **Figure** 5a). This capacitance for charge storage is captured by the Equation (3) reflecting the interplay between the overlapping area (A) of the two electrodes separated by distance (d), with ε representing the material's dielectric constant. This inclusion of a conductive filler significantly enhances the sensor's performance, resulting in a composite dielectric layer. Through capacitance measurement, we observed a significant increase in capacitance, validating the effectiveness of the composite dielectric layer.

$$C = \varepsilon_0 \varepsilon_a A/d \tag{3}$$

$$\frac{\Delta C}{C_0} = \frac{C - C_0}{C_0} = \frac{\varepsilon_0 \varepsilon_a (A/d)}{\varepsilon_0 \varepsilon_{a0} (A/d)} - 1 = \frac{\varepsilon_a}{\varepsilon_{a0}} - 1 \tag{4}$$

The capacitance (C) of a capacitor can be calculated using Equation (3), which provides a fundamental understanding of its behavior. However, when we introduce conductive fillers into the dielectric medium, Equation (4), becomes essential for interpreting the change in capacitance (ΔC). In Equation (4), ΔC represents the change in capacitance, C_0 signifies the baseline capacitance with the pristine dielectric layer, and d stands for the distance between the electrodes. Crucially, ε_a and ε_{a0} denote the dielectric constants of the composite and pristine dielectric layers, respectively.[18,79] Given the $\varepsilon_a > \varepsilon_{a0}$ from Equation (4), the variation in capacitance will increase. This increase in capacitance variation is verified by the plot in Figure 5a_1, where the C is observed to be larger than the baseline C_0. The key principle underlying this enhancement is that ε_a is greater than ε_{a0}, as shown from Equation (4). When $\varepsilon_a > \varepsilon_{a0}$, it signifies an increase in the dielectric constant of the composite material due to the presence of conductive fillers. This pivotal modification results in an amplified variation in capacitance.

The mechanism underlying the observed enhancement in capacitance is multifaceted and rooted in the intricate interplay of various factors. Conductive fillers, such as LM or carbon nanoparticles, exhibit exceptionally high permittivity compared to the surrounding dielectric material. When dispersed within the dielectric medium, these fillers contribute significantly to the overall dielectric constant (ε) of the composite material. Additionally, the introduction of patterned PVA droplets in the medium increases the effective surface area of the sandwiched device, thereby providing more surface area for charge storage. Given that the C of a capacitor is directly proportional to the ε and the effective surface area (A), this augmentation leads to a substantial increase in capacitance. Furthermore, conductive fillers create additional charge storage sites within the dielectric, which, upon external loading, contribute to the overall performance enhancement beyond its C_0, as depicted in Figure 5a_1. The comparative analysis between samples without LM ($w/o\ LM$), with LM spread uniformly ($w/\ LM\ -\ s$), and with patterned LM droplets ($w/\ LM\ -\ p$) underscores the pivotal role of both the distribution of conductive fillers and the geometric arrangement of the composite components in modulating the capacitance performance of the device.

In conjunction with the observed enhancement in capacitance, the response of these configurations is further elucidated through Figure 5a_2. Notably, the patterns of LM with PVA matrix serve dual roles as conductive fillers and microstructures, thereby influencing the elastic strain response of the composite material. However, polymers have a low young's modulus, high degree of stretchability, along with toughness, they can limit the sensitivity of these sensors, due to their unchanging volume. Various researchers have developed intricate internal geometries so called, microstructures, that proved to have higher relative capacitance change for shorter distances, with reduced dependance on the polymer's viscoelastic behavior for better reaction times. In our case LM patterns due to their fluidic nature can deform at low loading to sense strain. As depicted in Figure 5a_2 the sensors were loaded with 5 N, where the $w/\ LM\ -p$ demonstrated superior response.

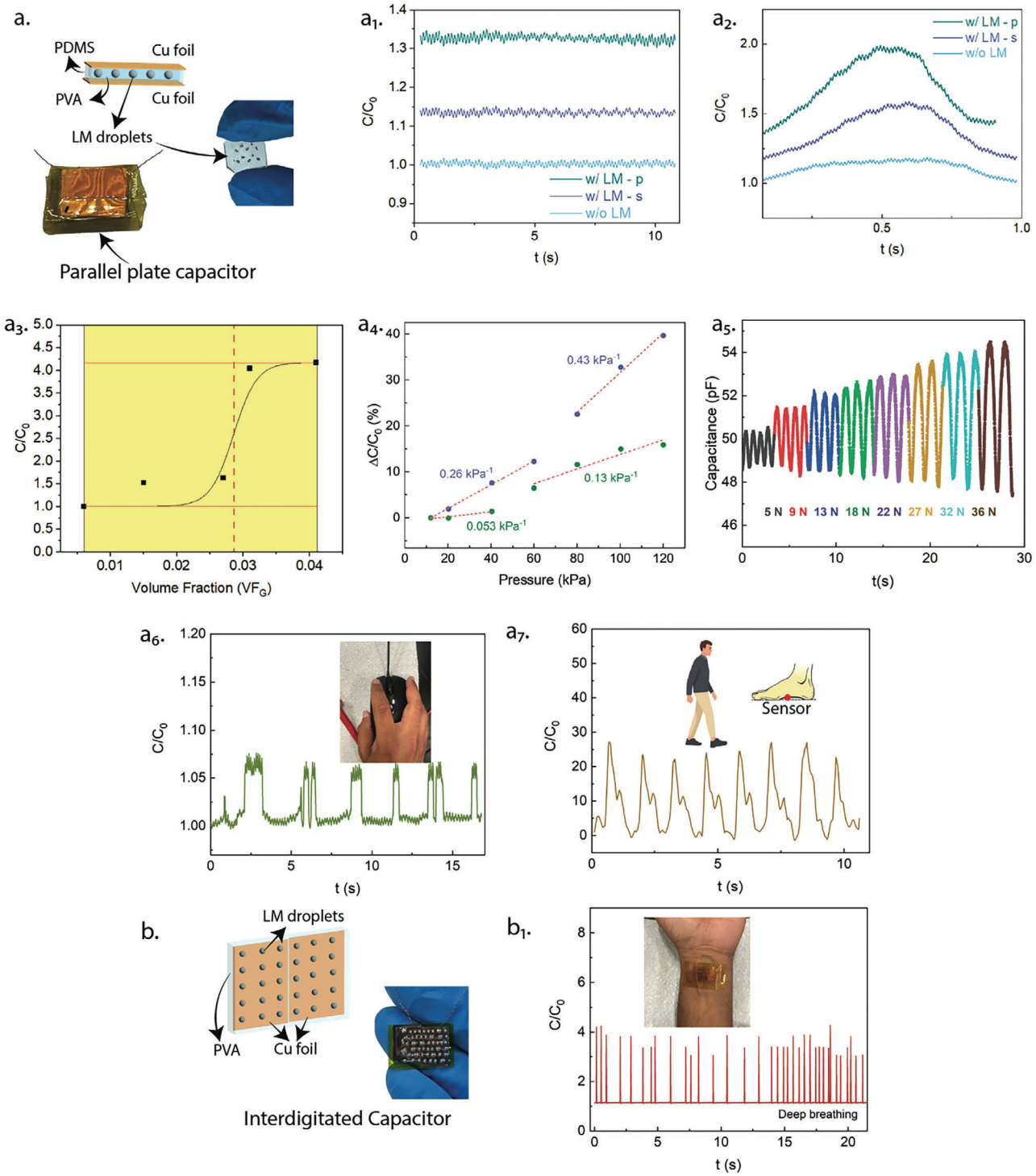

Figure 5. a) Schematic and digital images of the parallel plate capacitor and of the encapsulated droplets (600 µm diameter, with a volume fraction of obtained via the zig-zag printing motion that a_1) prompted an increase in inherent capacitance of the parallel plate capacitor, compared across three configurations, a_2) showing improved response, courtesy of LM inclusion and its patterns owing to the microstructural behavior. a_3) As the volume fraction of Ga (VF_G) in the patterns increased, the relative capacitance of the capacitor was also seen to increase, where the plot depicts the percolation due to the patterns, with dashed red line denoting the percolation threshold VF. The patterns with droplet spacing of 6.49, 3.68, and 1.43 mm, respectively, and Quad-dot and Hexa-dot correspond to the merged droplets −4 and 6 respectively were considered for the percolation threshold analysis. a_4) This is further visualized through the difference in sensitivity between 1.43 mm droplet-spaced pattern and the Quad-dot pattern. a_5) The recorded capacitance changes in response to compressive loading and unloading from 5 to 36 N, a_6) mouse click, and a_7) human motion with the sensor placed in the arch of the human foot. b) Schematic and digital images of the interdigitated capacitor b_1) making real-time and in-situ tested wrist artery pulse data through capacitive signal, with consistent signals in regular versus deep breathing.

In investigating the capacitive properties of LM – PVA composites, our study reveals a significant dependence of capacitance on the geometric configuration of LM droplets within a PVA matrix. This was observed using varying geometries of patterns as represented in Figure S15 (Supporting Information). As depicted in Figure 5a$_3$, the capacitance exhibits a gradual increase with decreasing droplet size, followed by a sharp rise as the volume fraction approaches a percolation threshold of $VF_G \approx 0.02858$. This observed behavior highlights the critical influence of droplet proximity and arrangement in augmenting electrical connectivity, thereby confirming the pivotal role of percolation in the transition from isolated conductive clusters to a cohesive conductive network. These insights are paramount for the design and optimization of responsive sensing materials, where precise control over the geometry of liquid metal patterns enables the attainment of desired sensing thresholds and response characteristics.

In the realm of capacitive pressure sensors, optimizing performance involves strategic adjustments to either the conductive fillers or the dielectric layer.[54,75] The term "uniformity" assumes significance, emphasizing the even distribution and consistent size of droplets and patterns within these layers, a crucial factor tailored for specific applications. As demonstrated in Figure 5a$_3$, the capacitive performance of the sensor increases with the availability of conductive fillers, transitioning from 6.49 mm droplet spacing to more closely spaced 1.43 mm configurations. This enhancement is attributed to the increasing VF_G in the patterns, leading to an effective augmentation in capacitance. Additionally, our findings align with the conventional understanding that an enhanced dielectric permittivity is associated with the formation of micro-capacitor networks.[80] Consequently, increasing the VF_G results in an increased dielectric constant of the dielectric medium due to the heightened availability of conductive EGaIn droplets. In regions between the droplets where the polymer resides, electric fields intensify owing to the migration and accumulation of charge carriers at the droplet-polymer interfaces, thereby significantly boosting the dielectric constant and enhancing capacitive performance. The sensitivity of the sensors was further elucidated by comparing the sensitivity of a merged sample (Quad-dot) with that of a 1.43 mm spaced pattern, as depicted in Figure 5a$_4$. Notably, the sensitivity of the Quad-dot configuration surpassed that of the spaced pattern, particularly at lower pressures. However, with increasing applied pressure, the responsivity of the sensor also increased, attributable to the reduced spacing between the electrode plates. Additionally, an observation was made regarding the sensitivity's augmentation with increasing pressure, attributed to the elastic deformation of the merged droplets, which contributes to a faster elastic response compared to the spaced pattern configuration.

To further demonstrate the capactive sensing performance, we delved into the sensor's response to external loading. Sensor with the$VF_G \approx 0.015$ was tested for capacitance variations under various loading conditions, ranging from 5 to 36 N (Figure 5a$_2$). As loading is increased gradually, the stress is transferred from the PDMS to the LM droplets. This stress tends to flatten the droplet exposing a more effective surface area. The capacitance response changed with the increase in pressure application. These values showed stable increments over loading and unloading cycles reverberating the reliable synergetic deformation. Notably, the sensor showcased remarkable sensitivity across this loading spectrum, ranging from ≈37.31 to 20.67 kPa^{-1}. It's important to note that the sensitivity declined with increased loading, which could be attributed to the elasticity of the PDMS, causing the electrodes to draw closer to the conductive fillers, thereby elevating capacitance. The sensitivity of the device can be attributed to the enhanced capacitive performance due to droplets increasing the available surface area, and the conformation at the LM/PDMS interface due to the oxide skin adherance, leading to the transfer of load.

Entering an era marked by personalized products and services, the demand for tailored solutions in healthcare and cybersecurity has surged dramatically.[81,82] As they displayed capable sensing over a wide range of pressure, these LM patterned devices can be poised to address this growing need by offering customization options that match the unique pressure profiles of individuals, making them integral components of connected security systems.[83] In today's common household computing environment, we envision the potential for individualized mouse click feedback systems, finely tuned to users' input characteristics, thereby holding immense promise for detecting early Alzheimer disease signs or anti-theft applications (Figure 5a$_6$). The realm of personalized healthcare monitoring has gained substantial attention, with applications spanning motion detection and heart rate monitoring. In this context, we've developed a straightforward and cost-effective motion detection sensor, strategically positioned near the front section of the foot, within the arch (Figure 5a$_7$). This thoughtful placement ensures that it neither disrupts the user's natural stride by creating uneven terrain nor increases the risk of sensor damage.

Furthermore, the encapsulated patterns offer versatility in applications such as the utilization of an interdigitated capacitor arrangement. Here, copper (Cu) electrode plates are separated by a narrow gap and connected via a dielectric material film. In Figure 5b, the Cu foils are linked by the composite PVA/LM pattern. When connected to a voltage source, the fringing field generated between the plates is disrupted, leading to an increase in capacitance when skin is introduced into the field, effectively grounding it. These configurations have found utility in diverse tasks, including monitoring wrist artery pulse rates, exploring droplet migration dynamics, and assessing effective capacitance (Figure 5b$_1$). Our innovative approach, combining LM patterning and flexible sensor design, opens doors to a wide range of applications, from personalized security systems to healthcare monitoring and beyond, promising transformative possibilities for the future.

3. Conclusion

In summary, our study introduces an innovative technique that revolutionizes the art of achieving versatile EGaIn patterning, harnessing its distinctive attributes of fluidity, high surface tension, and low viscosity. By seamlessly amalgamating multimaterial Direct-Ink-Writing with Cross Flow droplet generation, we have effectively deposited intricate EGaIn patterns, employing PVA both as the flow medium and packaging substrate. Our meticulous control over variables like traverse speed and feedstock flow pressure has led to the attainment of meticulous pattern periodicity, underscoring the innate adaptability of this methodology. The implications of our findings extend across

diverse domains, with the realm of capacitive pressure sensing standing out as a compelling application. Beyond its contribution to advancing LM patterning techniques, our pioneering method unfurls new avenues for the creation of highly functional devices and sensors endowed with expanded capabilities. The fusion of microfluidics and 3D printing in our approach presents scalable solutions that hold promise across a spectrum of industries. As we continue to delve into the potential of LM patterning, our work establishes a robust cornerstone for propelling innovation in electronics, soft robotics, and wearable sensing applications.

4. Experimental Section

Materials: Gallium-indium eutectic liquid metal (i.e., Ga 75.5%/ In 24.5%, ≥ 99.99 trace metals basis), hydrochloric acid (HCl. ACS reagent 37%, CAS #7647-01-0), and Dimethyl sulfoxide (DMSO) (American Chemical Society reagent, >99.8%, CAS #67-68-5) solvent were purchased from Sigma–Aldrich, USA and used as obtained. PVA (i.e., Kuraray Poval 40–88 with an average molecular weight (M_w) of ≈205,000 g mol^{-1}, partially hydrolyzed, CAS #9002-89-5) was provided by Kuraray. Transparent silicone elastomer (Dow Sylgard 184 Silicone Elastomer kit clear) was purchased from Krayden, Inc. 1,6-hexanediol diacrylate (HDDA, technical grade, 80%), 1-phenylazo-2-naphthol (Sudan I, dye content ≥95%), phenylbis (2,4,6-trimethyl benzoyl) phosphine oxide (Irgacure 819, 97%) were purchased from Sigma – Aldrich. 2-propanol (IPA, Certified ACS, Fisher Chemical) was purchased from Fisher–Scientific. All the materials were used as received.

Preparation of Feedstocks Before 3D Printing: A pair of feedstock materials were used to deposit the droplets in controlled patterns onto a glass slide substrate. Feedstock A was loaded with PVA/DMSO solution, and feedstock B was loaded with LM (Figure 1b). The latter was prepared by exposing the bulk material to oxidation via magnetic stirring over extended periods. LM (1–1.5 mL) was stirred at 500 RPM for over 15 min to ensure the continuous breaking and formation of oxide skin over the exposed area, reducing the effective surface tension of the LM (Figure S5, Supporting Information). A layer containing 2 mL, pH 4–5 HCl was added on top of LM to avoid further oxidation (Figure 2a). The feedstock A in the form of a solution was prepared with 10 wt% PVA/DMSO by constant magnetic stirring at 80 °C. Then the PVA/DMSO solutions were vacuum degassed at 60 °C with 30 in. of Hg pressure for up to 30 min to purge the air bubbles from the solution.

The feedstocks A and B were loaded into two separate polypropylene (PP) fluid dispensing syringe barrels and extruded using two individual digital fluid dispensers (i.e., Metcal DX-255, digital dispensing for low viscosity medium, 0–1.0 bar (i.e., 14 psi)) (Figure 1b; Figure S4, Supporting Information). The 3D printing platform used was based on an open-source 3D printing system (System 30 M from Hyrel 3D) with an enclosed build casing. The printer had a build volume of 225 mm × 200 mm × 200 mm in the x, y, and z directions. It had a 150+ MHz 32-bit ARM processor and a modular micro-stepping motor that provides positional accuracy of ± 50 µm in the X, Y, and 10 µm in the Z axis. A positional resolution of 5 µm in the X and Y axis and 1 µm in the Z axis.

Manufacturing Customized Nozzles: The 3D printing setup involves two variants of customized nozzles, namely, "NM" for non-merged and "M" for merged (Figure 1a), these were employed independently to produce different surface patterns. Each nozzle consists of two inlets for feedstocks A and B, and the inlets were differentiated by their geometry. The NM had a "non-merged" geometry for linear and continuous PVA/LM deposition (e.g., lines), and the "M" has a "merged" geometry benefiting dotted LM formation with varying packing factors (e.g., dots and lines) (Figure 1b). The geometry in NM ensures no contact between the two feedstocks (e.g., LM and PVA) until extruded, as the microfluidic channels don't intersect. In contrast, M allows the two materials to come in contact before being extruded (Figure S1, Supporting Information).

The microfluidic nozzles were designed on SolidWorks 2021 (CAD modeling software) and then sliced into a series of 2D images by a customized slicing program with a predefined layer thickness of 5 µm. Photocurable resins used to print these microfluidic nozzles were formulated with 97.6 wt% HDDA, 2 wt% Irgacure 819 as the photo-initiator, and 0.4 wt% Sudan I as the photo-absorber. The µCLIP 3D printing setup was in-house designed and constructed (Figure 1a) using a light engine (Pro4500, Wintech Digital) equipped with a 385 nm UV light source as well as a digital micrometer device (DMD, Texas Instruments) with a resolution of 1280 × 800 as the optical input, along with a UV lens (UV8040BK2, Universe Optics) to yield a lateral resolution of 6.9 × 6.9 $µm^2$ $pixel^{-1}$ and a maximum lateral printing area of 8.83 × 5.52 mm^2. Each sliced 2D image was generated and projected onto an oxygen-permeable thin film (Teflon AF2400, 40 µm nominal thickness, Biogeneral) mounted underneath a customized resin bath. The focusing status of the generated images was monitored using a CCD camera (MU2003-BI, AmScope). A z-axis motorized stage (X-LSM200A-KX13A, Zaber Technology Inc.) was used to control the movement of the printing platform, and a desktop computer was used to manage the entire printing procedure. After which, the samples were thoroughly rinsed in IPA and blow-dried.

Multimaterial Direct Ink Writing (DIW): The custom printheads (nozzles) feature dual feedstock channels (i.e., A – PVA and B – EGaIn) and were mounted onto a customized, 3D-printed holder (Figure 2f). This holder was connected to one of the printhead rails inside the 3D printer, allowing the setup to follow the imported G-code and achieve manufacturing autonomy (Figure 1). Each nozzle type was designed for a particular patterning and thus had fixed exterior dimensions (i.e., ≈1.75 mm in width and 4 mm in length at the top, 10 mm in height, and 250 µm at the bottom tip, Figure S1, Supporting Information). The starting inner diameter for each channel was designed to measure 1 mm with a draft angle of 5° to accommodate and arrest commercially available silicone feed tubes firmly (Figure S2, Supporting Information). The materials were fed to the nozzle via two silicone feed tubes (Figure S4, Supporting Information), connecting the nozzle with the reservoir syringe barrel. A combination of two pneumatic fluid dispensers (i.e., Metcal DX-255) was employed as the pressure delivery system.

Sensor Assembly: To address the sensing applications, two capacitive pressure sensing configurations were considered. The droplets were encapsulated in PDMS in order to stabilize their pattern and give them durability during operations. Encapsulated patterns were then sandwiched between two electrodes (Cu) foils as the terminals, making them the parallel plate capacitor configuration. Whereas, a second configuration, used the droplets confined in PVA attached by two closely spaced electrode plates (Cu), making them the interdigitated capacitor assembly. Copper wires were attached to each of the foils to facilitate further connections.

Characterization: *Rheology Tests*: The rheology of LM and the PVA/DMSO solution was studied using a 40 mm 2° Cone and Peltier plate rheometer (Discover hybrid rheometer DHR2, TA instruments). The viscoelastic behavior of eutectic Gallium Indium and the different concentrations of PVA dissolved in DMSO were studied at room temperature (RT) (≈23 °C). The viscosity was measured as a function of shear rate ranging from 0.1 – 1000 s^{-1}. Storage and loss modulus were measured as a function of angular frequency ranging from 0.1 – 100 rad s^{-1}.

Optical Imaging: The printed samples were analyzed under a 3D measurement macroscope (Keyence VR 3200 series, USA), allowing for surface imaging and printed pattern profilometry.

Capacitance Measurements: The capacitor was fabricated by peeling the patterns from the substrate and encapsulating them within PDMS. The first type of sensor followed a parallel plate capacitor configuration by sandwiching the encapsulated pattern between copper and aluminum. Later, the package was wrapped in Kapton tape to eliminate finger capacitance, and copper wires made up the terminals. The copper wires were connected to the terminals of the KEITHELEY DMM7510 7 ½ DIGIT multimeter.

Supporting Information

Supporting Information is available from the Wiley Online Library or from the author.

Acknowledgements

The authors thank the support from NSF EAGER (award # 1902172), NSF CAREER (award # 2145895), NSF GFRP (#1000375560), ONR NEPTUNE (award # N00014-22-1-2105), AFOSR (award # FA9550-22-1-0263), BSF (award # 2020102), Arizona Biomedical Research Commission (award # RFGA2022-010-07), and ACS PRF (award # 62371-ND10).

Conflict of Interest

The authors declare no conflict of interest.

Author Contributions

D.P. initiated the study by conceiving the idea and leading its evolution with vital input from S.L. and D.R. D.P. spearheaded the design and 3D printing of both merged and non-merged nozzles, along with performing characterization and demonstrative tests. S.L. played a crucial role in fabricating these nozzles using micro-CLIP technology. Assisting in the project, S.V.T. and Y.Z. focused on capacitive performance measurements, while T.T. conducted contact angle measurements to analyze hydrodynamic properties. The conceptual framework benefited from the insights of Y.G., G.M.-G., and A.A., with X.L. enhancing data analysis. Leadership and direction from X.C. and K.S. ensured the project's high standards and integrity. The manuscript, led by D.P. with support from S.L., D.R., and S.V.T., was a collaborative effort with contributions from all authors, who also reviewed and provided feedback, ensuring the study's comprehensive accuracy and integrity.

Data Availability Statement

The data that support the findings of this study are available from the corresponding author upon reasonable request.

Keywords

direct ink writing, droplet migration, eutectic gallium – indium, liquid metal, patterning

Received: March 27, 2024
Revised: May 13, 2024
Published online: June 8, 2024

[1] D. C. Kim, H. J. Shim, W. Lee, J. H. Koo, D.-H. Kim, *Adv. Mater.* **2020**, *32*, 1902743.
[2] J. J. Adams, E. B. Duoss, T. F. Malkowski, M. J. Motala, B. Y. Ahn, R. G. Nuzzo, J. T. Bernhard, J. A. Lewis, *Adv. Mater.* **2011**, *23*, 1335.
[3] C. B. Cooper, K. Arutselvan, Y. Liu, D. Armstrong, Y. Lin, M. R. Khan, J. Genzer, M. D. Dickey, *Adv. Funct. Mater.* **2017**, *27*, 1605630.
[4] M. D. Dickey, *Adv. Mater.* **2017**, *29*, 1606425.
[5] D. Qi, K. Zhang, G. Tian, B. Jiang, Y. Huang, *Adv. Mater.* **2021**, *33*, 2003155.
[6] L. Zhou, J. Fu, Q. Gao, P. Zhao, Y. He, *Adv. Funct. Mater.* **2020**, *30*, 1906683.
[7] C. Pan, K. Kumar, J. Li, E. J. Markvicka, P. R. Herman, C. Majidi, *Adv. Mater.* **2018**, *30*, 1706937.
[8] S. Pyo, J.-I. Lee, M.-O. Kim, T. Chung, Y. Oh, S.-C. Lim, J. Park, J. Kim, *J. Micromech. Microeng.* **2014**, *24*, 075012.
[9] E. O. Polat, G. Mercier, I. Nikitskiy, E. Puma, T. Galan, S. Gupta, M. Montagut, J. J. Piqueras, M. Bouwens, T. Durduran, *Sci. Adv.* **2019**, *5*, aaw7846.
[10] W. Jung, G. R. Koirala, J. S. Lee, J. U. Kim, B. Park, Y. J. Jo, C. Jeong, H. Hong, K. Kwon, Y. Ye, *ACS Nano* **2022**, *16*, 21471.
[11] C. Ladd, J.-H. So, J. Muth, M. D. Dickey, *Adv. Mater.* **2013**, *25*, 5081.
[12] S. Handschuh-Wang, T. Gan, T. Wang, F. J. Stadler, X. Zhou, *Langmuir* **2021**, *37*, 9017.
[13] J.-H. Kim, S. Kim, J.-H. So, K. Kim, H.-J. Koo, *ACS Appl. Mater. Interfaces* **2018**, *10*, 17448.
[14] B. Fernandes Azevedo, L. Barros Furieri, F. M. Peçanha, G. A. Wiggers, P. Frizera Vassallo, M. Ronacher Simões, J. Fiorim, P. Rossi de Batista, M. Fioresi, L. Rossoni, I. Stefanon, M. J. Alonso, M. Salaices, D. Valentim Vassallo, *J. Biomed. Biotechnol.* **2012**, *2012*, 949048.
[15] D. Wang, X. Wang, W. Rao, *Acc. Mater. Res.* **2021**, *2*, 1093.
[16] E. J. Markvicka, M. D. Bartlett, X. Huang, C. Majidi, *Nat. Mater.* **2018**, *17*, 618.
[17] J. Yan, Y. Lu, G. Chen, M. Yang, Z. Gu, *Chem. Soc. Rev.* **2018**, *47*, 2518.
[18] E. Bury, A. S. Koh, *ACS Appl. Mater. Interfaces* **2022**, *14*, 13678.
[19] J. Meng, Y. Zhang, X. Zhou, M. Lei, C. Li, *Nat. Commun.* **2020**, *11*, 3716.
[20] D. Zhang, Y. Zhong, Y. Wu, X. Zhang, M. D. Dickey, J. Yang, *Compos. Sci. Technol.* **2021**, *216*, 109066.
[21] H. Wang, R. Li, Y. Cao, S. Chen, B. Yuan, X. Zhu, J. Cheng, M. Duan, J. Liu, *Adv. Fiber Mater.* **2022**, *4*, 987.
[22] X. Li, M. Li, L. Zong, X. Wu, J. You, P. Du, C. Li, *Adv. Funct. Mater.* **2018**, *28*, 1804197.
[23] T. V. Neumann, E. G. Facchine, B. Leonardo, S. Khan, M. D. Dickey, *Soft Matter* **2020**, *16*, 6608.
[24] Z. Chen, J. B. Lee, *ACS Appl. Mater. Interfaces* **2019**, *11*, 35488.
[25] D. Kim, P. Thissen, G. Viner, D.-W. Lee, W. Choi, Y. J. Chabal, J.-B. Lee, *ACS Appl. Mater. Interfaces* **2013**, *5*, 179.
[26] M. Kim, D. K. Brown, O. Brand, *Nat. Commun.* **2020**, *11*, 1002.
[27] B. A. Gozen, A. Tabatabai, O. B. Ozdoganlar, C. Majidi, *Adv. Mater.* **2014**, *26*, 5211.
[28] C. W. Park, Y. G. Moon, H. Seong, S. W. Jung, J.-Y. Oh, B. S. Na, N.-M. Park, S. S. Lee, S. G. Im, J. B. Koo, *ACS Appl. Mater. Interfaces* **2016**, *8*, 15459.
[29] M. Kim, H. Alrowais, S. Pavlidis, O. Brand, *Adv. Funct. Mater.* **2017**, *27*, 1604466.
[30] S. Liu, M. C. Yuen, E. L. White, J. W. Boley, B. Deng, G. J. Cheng, R. Kramer-Bottiglio, *ACS Appl. Mater. Interfaces* **2018**, *10*, 28232.
[31] R. Guo, Y. Zhen, X. Huang, J. Liu, *Appl. Mater. Today* **2021**, *25*, 101236.
[32] A. Mitra, K. Xu, S. Babu, J. H. Choi, J.-B. Lee, *Adv. Mater. Interfaces* **2022**, *9*, 2102141.
[33] Y. Huang, N. Bu, Y. Duan, Y. Pan, H. Liu, Z. Yin, Y. Xiong, *Nanoscale* **2013**, *5*, 12007.
[34] Y. Hou, F. Wang, C. Qin, S. Wu, M. Cao, P. Yang, L. Huang, Y. Wu, *Nat. Commun.* **2022**, *13*, 7625.
[35] S. Tagliaferri, A. Panagiotopoulos, C. Mattevi, *Mater. Adv.* **2021**, *2*, 540.
[36] A. Haake, R. Tutika, G. M. Schloer, M. D. Bartlett, E. J. Markvicka, *Adv. Mater.* **2022**, *34*, 2200182.
[37] P. Jiang, Z. Ji, X. Zhang, Z. Liu, X. Wang, *Prog. Addit. Manuf.* **2018**, *3*, 65.
[38] T. V. Neumann, M. D. Dickey, *Adv. Mater. Technol.* **2020**, *5*, 2000070.
[39] M. Rahimi, A. Shams Khorrami, P. Rezai, *Colloids Surf., A* **2019**, *570*, 510.
[40] S. Hettiarachchi, G. Melroy, A. Mudugamuwa, P. Sampath, C. Premachandra, R. Amarasinghe, V. Dau, *Sens. Actuators, A* **2021**, *332*, 113047.
[41] J. R. Tumbleston, D. Shirvanyants, N. Ermoshkin, R. Janusziewicz, A. R. Johnson, D. Kelly, K. Chen, R. Pinschmidt, J. P. Rolland, A. Ermoshkin, *Science* **2015**, *347*, 1349.
[42] R. Janusziewicz, J. R. Tumbleston, A. L. Quintanilla, S. J. Mecham, J. M. DeSimone, *Proc. Natl. Acad. Sci. USA* **2016**, *113*, 11703.

[43] P. Zhu, L. Wang, *Lab Chip* **2017**, *17*, 34.
[44] T. Cole, K. Khoshmanesh, S.-Y. Tang, *Adv. Intell. Syst.* **2021**, *3*, 2000275.
[45] T. Shay, O. D. Velev, M. D. Dickey, *Soft Matter* **2018**, *14*, 3296.
[46] S. Cheng, Z. Wu, *Lab Chip* **2012**, *12*, 2782.
[47] Y. Peng, H. Liu, Y. Xin, J. Zhang, *Matter* **2021**, *4*, 3001.
[48] J. Ma, F. Krisnadi, M. H. Vong, M. Kong, O. M. Awartani, M. D. Dickey, *Adv. Mater.* **2022**, *35*, 2205196.
[49] M. Song, K. E. Daniels, A. Kiani, S. Rashid-Nadimi, M. D. Dickey, *Adv. Intell. Syst.* **2021**, *3*, 2100024.
[50] G. Li, M. Parmar, D.-W. Lee, *Lab Chip* **2015**, *15*, 766.
[51] G. J. Hayes, J.-H. So, A. Qusba, M. D. Dickey, G. Lazzi, *IEEE Trans. Antennas Propag.* **2012**, *60*, 2151.
[52] D.-H. Kim, J.-H. Ahn, W. M. Choi, H.-S. Kim, T.-H. Kim, J. Song, Y. Y. Huang, Z. Liu, C. Lu, J. A. Rogers, *Science* **2008**, *320*, 507.
[53] T. J. Ober, D. Foresti, J. A. Lewis, *Proc. Natl. Acad. Sci. USA* **2015**, *112*, 12293.
[54] X. Li, J. M. Zhang, X. Yi, Z. Huang, P. Lv, H. Duan, *Adv. Sci.* **2019**, *6*, 1800730.
[55] J. Thelen, M. D. Dickey, T. Ward, *Lab Chip* **2012**, *12*, 3961.
[56] A. Yamaguchi, Y. Mashima, T. Iyoda, *Angew. Chem., Int. Ed.* **2015**, *54*, 12809.
[57] E. S. Elton, T. C. Reeve, L. E. Thornley, I. D. Joshipura, P. H. Paul, A. J. Pascall, J. R. Jeffries, *J. Rheol.* **2020**, *64*, 119.
[58] J. Lee, S. Jung, W. Kim, *Extreme Mech. Lett.* **2021**, *48*, 101386.
[59] T. Gan, W. Shang, S. Handschuh-Wang, X. Zhou, *Small* **2019**, *15*, 1804838.
[60] J.-E. Park, H. S. Kang, M. Koo, C. Park, *Adv. Mater.* **2020**, *32*, 2002178.
[61] M. D. Dickey, R. C. Chiechi, R. J. Larsen, E. A. Weiss, D. A. Weitz, G. M. Whitesides, *Adv. Funct. Mater.* **2008**, *18*, 1097.
[62] T. Hutter, W.-A. C. Bauer, S. R. Elliott, W. T. S. Huck, *Adv. Funct. Mater.* **2012**, *22*, 2624.
[63] K. Z. Hossain, M. Monwar, M. R. Khan, *Soft Matter* **2023**, *19*, 3199.
[64] A. R. Jacob, D. P. Parekh, M. D. Dickey, L. C. Hsiao, *Langmuir* **2019**, *35*, 11774.
[65] Z. Zhao, S. Soni, T. Lee, C. A. Nijhuis, D. Xiang, *Adv. Mater.* **2023**, *35*, 2203391.
[66] U. Daalkhaijav, O. D. Yirmibesoglu, S. Walker, Y. Mengüç, *Adv. Mater. Technol.* **2018**, *3*, 1700351.
[67] Z. J. Farrell, C. Tabor, *Langmuir* **2018**, *34*, 234.
[68] G. Chen, X. Deng, L. Zhu, S. Handschuh-Wang, T. Gan, B. Wang, Q. Wu, H. Fang, N. Ren, X. Zhou, *J. Mater. Chem. A* **2021**, *9*, 10953.
[69] R. J. Larsen, M. D. Dickey, G. M. Whitesides, D. A. Weitz, *J. Rheol.* **2009**, *53*, 1305.
[70] M. R. Khan, C. Trlica, M. D. Dickey, *Adv. Funct. Mater.* **2015**, *25*, 671.
[71] J.-H. So, H.-J. Koo, M. D. Dickey, O. D. Velev, *Adv. Funct. Mater.* **2012**, *22*, 625.
[72] D. Vella, L. Mahadevan, *Am. J. Phys.* **2005**, *73*, 817.
[73] I. A. Larmour, G. C. Saunders, S. E. Bell, *Angew. Chem.* **2008**, *120*, 5121.
[74] C. Zhao, L. Cai, M. Nie, L. Shang, Y. Wang, Y. Zhao, *Adv. Sci.* **2021**, *8*, 2004184.
[75] S. R. A. Ruth, V. R. Feig, H. Tran, Z. Bao, *Adv. Funct. Mater.* **2020**, *30*, 2003491.
[76] Y. Wan, Z. Qiu, Y. Hong, Y. Wang, J. Zhang, Q. Liu, Z. Wu, C. F. Guo, *Adv. Electron. Mater.* **2018**, *4*, 1700586.
[77] C. Pang, J. H. Koo, A. Nguyen, J. M. Caves, M.-G. Kim, A. Chortos, K. Kim, P. J. Wang, J. Tok, Z. Bao, *Adv. Mater.* **2014**, *27*, 634.
[78] M. D. Bartlett, A. Fassler, N. Kazem, E. J. Markvicka, P. Mandal, C. Majidi, *Adv. Mater.* **2016**, *28*, 3726.
[79] O. Atalay, A. Atalay, J. Gafford, C. Walsh, *Adv. Mater. Technol.* **2018**, *3*, 1700237.
[80] B. Li, C. A. Randall, E. Manias, *J. Phys. Chem. C* **2022**, *126*, 7596.
[81] Y. Yu, J. Li, S. A. Solomon, J. Min, J. Tu, W. Guo, C. Xu, Y. Song, W. Gao, *Sci. Rob.* **2022**, *7*, abn0495.
[82] S. Konishi, H. Kosawa, *Sci. Rep.* **2020**, *10*, 12038.
[83] K. Boukheddaden, M. H. Ritti, G. Bouchez, M. Sy, M. M. Dirtu, M. Parlier, J. Linares, Y. Garcia, *J. Phys. Chem. C* **2018**, *122*, 7597.